A Rough–Terrain, Casting Robot for the ESA Lunar Robotics Challenge

Simone Alicino, Manuel Catalano, Fabio Bonomo, Felipe A. W. Belo,
Giorgio Grioli, Riccardo Schiavi, Adriano Fagiolini, and Antonio Bicchi

***Abstract*— This paper describes the design and implementation of DAVID, a lunar vehicle developed for the European Space Agency (ESA) Lunar Robotics Challenge, presenting severe terrain negotiation and sample acquisition challenges. We discuss in some detail two of the main innovative aspects of our entry to the challenge, i.e. the locomotion system and the sample acquisition system.**

Motivated by the challenge specifications, a range of different locomotion systems were considered, among which we chose a simple, rugged and effective wheeled system. We provide an account of the choice of five different types of wheels, which were designed, analyzed and experimentally tested in conditions similar to the challenge. The system eventually turned out to be very effective in negotiating 89% slopes of volcanic terrain on the challenge site, Mount Teide in Tenerife.

To reduce the distance to be traveled on the difficult terrain and avoid risks in reaching the lowest parts of a crater, the vehicle was endowed with an innovative sample acquisition system, i.e. a casting manipulator. Casting manipulation is a technique in which the end-effector is thrown, the sample material is acquired, and the end-effector is retrieved using a light tether that acts as a "fishing line". The casting manipulator developed for DAVID uses an innovative sling-like technique, capable to obtain longer and more precise casts than previous oscillating versions. The analysis and experimental verification of DAVID's robot sling are reported, demonstrating its effectiveness.

Finally, we give a brief account of the outcomes of the ESA Lunar Robotics Challenge, where our team came in second over other 8 teams that passed the final qualification phase.

I. Introduction

In October 2008, the European Space Agency (ESA) carried out the ESA Lunar Robotics Challenge (LRC), designed to motivate and accelerate the research and development of tele-operated lunar rovers. The competitive characterization of the challenge proved successful in stimulating a solid volume of research from universities into lunar vehicles research. The short term objective of the challenge was the design of a robotic vehicle capable of retrieving soil samples from a lunar-like crater through remote operation. For that the challenge was held at the Minas de San Jose in the National Park of Teide on the Island of Tenerife, given its moon-crater-like terrain profile (see Fig. 1).

The challenge presented by the competition involved the development of a robotic vehicle that can deal with a lunar like terrain and overcome inherent difficulties in conditions of restrictive energy availability. In particular, the mobile robot should be able to accomplish a compound task consisting of climbing up the rim of a crater, descend down into the crater to locate and collect at least 100 g of selected soil material, and return back to the landing site. The two main design challenges were the development of the locomotion and the sample acquisition system. Therefore, the University of Pisa developed a six–wheeled rover with an innovative soil sample acquisition approach.

Authors are with the Interdepart. Research Center "Enrico Piaggio", University of Pisa, Via Diotisalvi, 2, 56100 Pisa, Italy. Phone: +39 050 553639. Fax: +39 050 550650.

Fig. 1. Picture of the Challenge Site at Minas de San José in Tenerife Island.

In order to achieve a larger working space, we propose a casting and retrieving system based on the casting manipulation technique [1]. The system is novel with respect to already proposed techniques [1], [4] because here the casting manipulator throws the end-effector with a circular horizontal movement, such as that of a sling, instead of using a vertical oscillatory movement as proposed in previous articles. The new approach leads to a completely different technique of casting manipulation, capable of obtaining longer and more precise results.

The paper is organized as follows. Section II provides a review of the competition challenges. More precisely, Section II-A and Section II-B describe a set of technical specifications for the locomotion and the sample acquisition systems, respectively, for which viable solutions are described in Section III. Then, Section IV presents the system's setup and shows its performance through experiments. Finally, the concluding Section V reports the results of the Challenge and comments on some expertise that we have gained through participation in it.

II. Problem Requirements

A. Locomotion System Problem

Design of the locomotion system has to consider a number of technical problems that are listed below. These involve

- **soil composition**: the crater soil is very abrasive and composed of granular loose material, ranging from fine dust grains to particles of up to few centimeters. Its chemical composition is silica based. The terrain profile presents fluid–like behavior and is able to provide very low traction, due to low humidity and soil granular variety.
- **environment**: the path from the landing site and the crater is a continuous slope of smooth terrain profile (roughness) and approximately 50 m distance. Access to inside the crater is determined by corridors with different inclinations. These corridors can be comprehended of unconsolidated slopes with inclinations of up to 40 degrees. Given the soil characteristics, slides can occur whenever the soil is loaded, and hence, descending/ascending the slopes poses an essential role in the design of locomotion of the robotics means. The crater features obstacles (rocks) of sizes that vary from 0.1 m to 0.5 m, which do not present a major locomotion problem given that paths around the obstacles are viable even though at the expense of time. Moreover, obstacles are contained in a relatively small area. Inside the crater there is a 20x40 m flat zone with a varied distribution of small positive and negative slopes of relatively smooth profile.
- **maximum allowed weight**: the maximum allowed system weight is 100 kg. Particular attention to weight distribution is an important factor during crater's ascending/descending tasks.
- **maximum allowed volume**: the maximum allowed occupancy of the robot, when stowed, is 0.5 m^3.
- **power consumption**: the maximum power consumption is limited to 2 kW, and a minimum autonomy of two hours is required.

B. Soil Acquisition Problem

One of the main objectives of the mission is the acquisition of at least 100 g of selected soil specimens from the bottom of the crater. Soil samples are granular and of sizes that vary from dust grains to pebbles. Selected soil samples are inside a delimited and visually distinctive area, and should be detected by the robot's operator via cameras. Once the material is found, it must be acquired and brought back to the landing site.

To accomplish this, the possibility of reaching large workspaces affords great potential advantages. State–of–the–art solutions to operate on objects at distances several times larger than the physical dimensions of the robot involve mobile platforms equipped with articulated arms [5]. Notwithstanding, pure wheeled or legged robotic locomotion systems depend heavily on the characteristics of the terrain, are forced to trade between speed of execution for robustness and terrain asperities, and above all use almost all the robot's energy for its motion. On the other hand, the alternative of building arms with either very long links, such as the Canadarm [6], seems to be applicable only in some very specific cases - for instance in the absence of gravity - and yet would not be possible here due to the space limitation of $0.5m^3$. Therefore, to reduce the energy effort for accomplishing the mission, we employ an end-effector casting and retrieving system. The mechanism is based on the casting manipulation technique [1], allowing an end-effector to be deployed at large distances from the robot's base by throwing (casting) it. A tether cable, that links the end-effector to the robotic device, is used to retrieve the end–effector. The operating phases of casting manipulation comprise a startup phase, a casting phase, and a retrieving phase. A casting manipulator mounted onboard the mobile platform can easily reach several meters from its base. Thus, its exploitation can indeed reduce the path to be travelled by the robot and even avoid a full descent of the crater.

III. Proposed Solution

A. Locomotion System

The development of a traction system for unstructured environments must trade–off among various factors, such as traction skill, maneuverability, obstacle negotiation, and system's reliability. For a competition such as the ESA LRC, reliability is the main aspect to be considered. Moreover, in our specific situation traction has a crucial role, especially during the climbing phase. Based on these considerations, the solution we propose is composed of a rigid frame and six independently actuated rigid wheels with lugs. The rigid frame simplifies the structure, makes it more reliable, provides a stable support for the casting manipulator. The 6 wheels, three of which are placed on each side of the vehicle, allow the rover to overcome obstacles of dimensions comparable to the rocks inside the crater, and they give good climbing performance. Positioning, size and shape of the wheels have been studied as they play an important role in the locomotion system. In the remainder of this section, we present the adopted model for traction, and we discuss obstacle negotiation and the robot's maneuverability.

1) Traction: The ability of a rover to attain sufficient traction to move the rover itself heavily depends on its wheel system [3]. Almost all available models require accurate knowledge of the terrain which include parameters such as cohesiveness, frictional moduli of deformation, moisture content, density, and viscosity. In the spirit of the challenge, only very uncertain data concerning the terrain morphology were given, and thus only rough measures of these parameters were available.

A widely accepted tire–terrain interaction model for rigid wheels with lugs is proposed in [7], where the forces and moments acting on the tire under steady–state conditions are considered to be entirely due to the normal pressure and the shear stress acting on the wheel–terrain interface. These two quantities are related to the external load acting on the wheel in the calculation of the drawbar pull F_d, defined as [2]:

$$F_d = F - R_t$$

where F is the thrust force determined by integrating the horizontal component of the shear stress over the contact

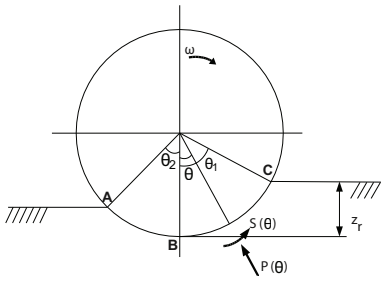

Fig. 2. Model of tire–terrain interaction for a rigid wheel.

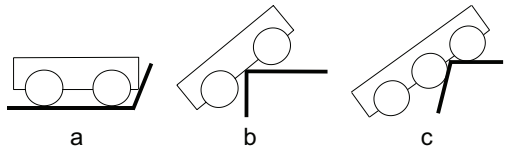

Fig. 3. a) Nose-in failure, b) Hang–up failure, c) A 6–wheeled robot can better negotiate the hang–up failure.

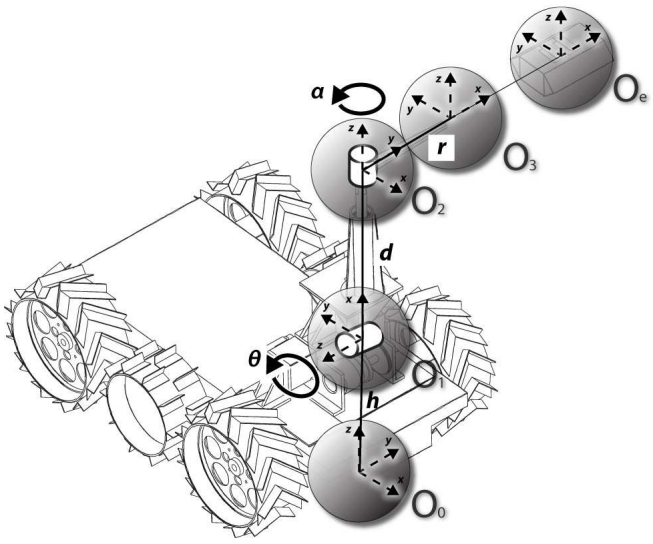

Fig. 4. Depiction of the casting manipulator on top of the mobile platform.

area and is given by

$$F = \frac{b_{tr} D}{2} \left[\int_0^{\theta_1} S(\theta) \cos\theta d\theta - \int_0^{\theta_2} S(\theta) \cos\theta d\theta \right] ,$$

and R_t is the motion resistance due to tire–terrain interaction determined by integrating the horizontal component of the normal pressure over the contact patch and is given by

$$R_t = \frac{b_{tr} D}{2} \left[\int_0^{\theta_1} P(\theta) \sin\theta d\theta - \int_0^{\theta_2} P(\theta) \sin\theta d\theta \right] ,$$

where D and b_{tr} are the wheel's diameter and width, respectively, and θ, θ_1, θ_2, $S(\theta)$ and $P(\theta)$ are as in Fig. 2. In particular, the shear stress $S(\theta)$ and the normal pressure $P(\theta)$ depend on the sinkage z_r. Moreover, the drawbar pull is influenced also by the slip $s = \frac{v_0 - v}{v_0}$, where v is the forward component of a wheel's speed, and v_0 is its peripheral speed. The slip represents an energy dissipation reducing the vehicle efficency and typically ranges between 20% and 40%.

2) Obstacles negotiation: The robot's ability to overcome obstacles, such as the ones that can be found in the Challenge site, can be studied within the framework considered in [3]. Among the various types of failure, we focused on the two which are most likely to occur, so–called *nose–in* and *hang–up* failure (see Fig. 3–(**a**, **b**)). These undesirable situations have been avoided by considering the size of the obstacles, the wheels' diameter and their number. Fig. 3–**c** shows that a 6–wheeled rover can better negotiate the hang–up failure. However, due to traction limitations, the hang–up failure can still occur if the robot's center of gravity is not shifted past the apex of the obstacle. This poses a further constraint in the robot's design that imposes that its center of gravity is shifted toward the leading axle, which we have obtained by placing the casting manipulator and all the batteries in the robot's front.

3) Maneuverability: The ability of the rover to follow a path depends on the vehicle's encroachment upon free space (see e.g. [3]), which we have verified through experiments.

B. Casting and Retrieval System

The structure of the casting manipulator is depicted in Fig. 4 and consists of a rigid link L_1 with a revolute joint $q_1 = \theta$, a rigid link L_2 with a revolute joint $q_2 = \alpha$, a tether cable departing from L_2 and an end-effector attached to the cable itself. Its configuration is described by $q = (\theta, \alpha, l)$, where θ represents the tilt angle and α the throwing angle, and l is the length of the cable. Its operation consists of the following phases:

- **startup**: the arm is lifted up to the desired tilt angle θ and the end–effector is accelerated until a desired speed $\dot{\alpha}$ is reached;
- **casting**: at a suitable throwing angle $\bar{\alpha}$, the clutch is released and the end–effector is thrown tangent to L_2's movement;
- **sample retrieval**: at a suitable landing instant, the clutch is engaged and the end–effector is dredged in order to collect a sample of material; finally, the end–effector itself is retrieved by rewinding the cable.

During the startup phase, the tilt angle is kept constant, i.e., $\dot{\theta} = 0$, and, as the cable is completely winded, we assume that the end-effector's frame is coincident to the frame of L_2, i.e., $O_3 = O_e$. During the casting phase instead, the end–effector dynamics can be studied independently from the manipulator configuration. Therefore, in order to solve the end-effector flight trajectory, its initial state is determined by the differential kinematics of the manipulator during startup phase, and ballistic flight is described by the end–effector dynamics equations during the casting phase.

1) Direct and Differential Kinematics: The position p_e of the end–effector w.r.t. a base frame attached to the robot's

base can be extracted from the robot's direct kinematics

$$\begin{aligned} T(q) &= T_1(\hat{z},h)\,T_2(\hat{y},\theta)\,T_3(\hat{x},i_{ax})\,T_4(\hat{z},d) \\ &\quad T_5(\hat{z},\alpha)\,T_6(\hat{x},r)\,T_7(\hat{z},\beta)\,T_8(\hat{y},\gamma)\,T_9(\hat{x},l)\,, \end{aligned}$$

where h, r, d are constant parameters reported in the figure, and i_{ax} and γ are two construction displacements. Direct computation of $T(q)$ gives $p_e(q) = (x_e, y_e, z_e)$ with

$$\begin{aligned} x_e &= (c_\theta\, c_\alpha\, c_\beta - c_\theta\, s_\alpha\, s_\beta)\, c_\gamma\, l - s_\theta\, s_\gamma\, l + \\ &+ c_\theta\, r\, c_\alpha + c_\theta\, i_{ax} + s_\theta\, d\,, \\ y_e &= s_\alpha\, c_\beta\, c_\gamma\, l + c_\alpha\, s_\beta\, c_\gamma\, l + r\, s_\alpha\,, \\ z_e &= (-s_\theta\, c_\alpha\, c_\beta + s_\theta\, s_\alpha\, s_\beta)\, c_\gamma\, l - c_\theta\, s_\gamma\, l + \\ &- s_\theta\, r\, c_\alpha - s_\theta\, i_{ax} + c_\theta\, d + h\,. \end{aligned}$$

The end–effector's speed can be computed by the robot's differential kinematics, that can be obtained as

$$\dot{p}_e(q) = \frac{\partial p_e(q)}{\partial q}\,\dot{q} = J(q)\,\dot{q}\,,$$

where $J(q)$ is the *robot's Jacobian*, and $\dot{q} = (\dot{\theta}, \dot{\alpha}, \dot{l})^T$. Having denoted with $\omega = \dot{\alpha}$ the angular speed of the second joint, with $v = \dot{l}$ the linear velocity of the third joint, and having $\dot{\theta} = 0$, the computation gives the result

$$\begin{aligned} \dot{x}_e &= -c_\theta\,(s_\alpha\, c_\beta + c_\alpha\, s_\beta)\, c_\gamma\, l\, w + \\ &- (c_\theta\, c_\alpha\, s_\beta + c_\theta\, s_\alpha\, c_\beta)\, v\,, \\ \dot{y}_e &= (c_\theta\,(c_\theta\, c_\alpha\, c_\beta - c_\theta\, s_\alpha\, s_\beta)\, c_\gamma\, l - s_\theta\, s_\gamma\, l + \\ &- s_\theta\,(-s_\theta\, c_\alpha\, c_\beta + s_\theta\, s_\alpha\, s_\beta)\, c_\gamma\, l - c_\theta\, s_\gamma\, l)\, w + \\ &- (s_\alpha\, s_\beta - c_\alpha\, c_\beta)\, v\,, \\ \dot{z}_e &= s_\theta\,(s_\alpha\, c_\beta + c_\alpha\, s_\beta)\, c_\gamma\, l\, w + (s_\theta\, c_\alpha\, s_\beta + s_\theta\, s_\alpha\, c_\beta)\, v\,. \end{aligned}$$

2) Dynamics: The dynamics of the end–effector during the casting phase can be determined by considering the end–effector itself as a mass point, subject to a friction force F_i generated by the clutch and transmitted through the cable. Assuming that the cable is never loose, the friction is $F_i = (\tau/\rho)\,\hat{p}_e$, where τ is a resistant torque due to the residual friction present between the stator and the rotor of the clutch, ρ is its radius, and $\hat{p}_e = (\hat{x}_e, \hat{y}_e, \hat{z}_e)^T = \frac{p_e - p_3}{\|p_e - p_3\|}$ that is aligned with the cable. Then, the end–effector's dynamics reads

$$\left\{ \begin{array}{rcl} \left(\frac{I}{\rho^2} + m\right)\,\ddot{x}_e(t) &=& \frac{\hat{x}_e(t)}{\rho}\,\tau\,, \\ \left(\frac{I}{\rho^2} + m\right)\,\ddot{y}_e(t) &=& \frac{\hat{y}_e(t)}{\rho}\,\tau\,, \\ \left(\frac{I}{\rho^2} + m\right)\,\ddot{z}_e(t) &=& -m\,g + \frac{\hat{z}_e(t)}{\rho}\,\tau\,. \end{array} \right. \quad (1)$$

IV. Experimental Validation of the System

Validation and performance evaluation of the traction systems above presented and based on different kind of wheels have been achieved through experiments. Effectiveness of the casting and retrieval system has also been successfully confirmed through experiments. This section describes the setup of the overall robotic system and experimental results.

A. Experimental Setup

- **embedded controller**: a National Instruments CompactRIO (cRIO-9014) has been used with modules for analog input, analog output, digital I/O, 2 port CAN Bus, 8 RS232 ports, and relays;

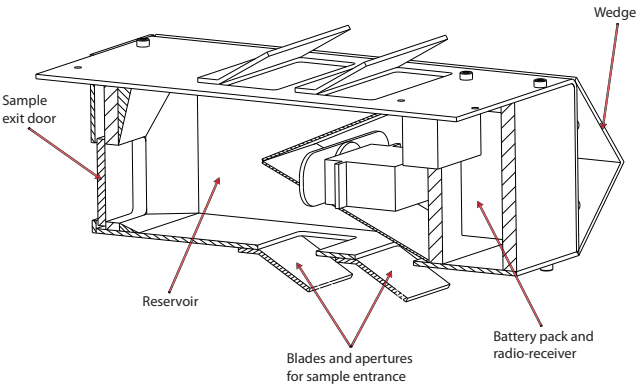

Fig. 5. Cross–section of the end-effector.

- **locomotion system**: It is comprised of four PR-90 and two PR-70 Schunk Power Cube motors. A PAE130 Terminal Block board is responsible for powering the motors and as a protection to the CAN-bus interface.
- **casting system**: It is composed of a support frame, a hollow vertical shaft and a counterbalanced rigid arm, representing the first and the second links, respectively. The first joint is actuated by a Schunk PR90 motor linked to the support frame. The rigid arm is integral with the vertical shaft, that is actuated by a Schunk PDU90 motor. The shaft and the motor are linked together by a reduction gear of ratio $1/3$ to increase the angular velocity. The cable is winded around a reel mounted on an electromagnetic clutch. The reel is mounted on the rotor of the clutch that is keyed on a shaft integral with a Schunk PR70 motor. The cable passes inside the shaft, driven by some pulleys to reduce friction, and reaches the end of the rigid arm, where it is linked to the end-effector. The structure is made of aluminum alloy to minimize weight. The cable is made of polyethylene fiber in order to be light and resistant. The end-effector consists of a rectangular box presenting two apertures on each large face (see Fig. 5). The two other faces are equipped with wedges, to tilt the end-effector and make it fall upon a large face. When the end-effector is pulled, the sample material is driven inside the reservoir by mean of blades. Once the material is collected, a radio–controlled servomotor installed inside the box moves two walls closing the apertures. In this way no more material can enter, and no material can come out of the reservoir. To release the sample material a further tele-controlled servomotor opens a little door at the bottom of the reservoir, so that the material can flow out driven by some slopes;
- **vision and laser system**: It is composed of an Imaging Source DFK21AF04-Z color camera with mechanical zoom; 2 DBK24AF04 color cameras; an Acuity Laser Measurement AR1000 laser; and an Acuity Research PTU-46 pan-tilt; Camera acquisition is done through National Instruments Compact Vision System (CVS).

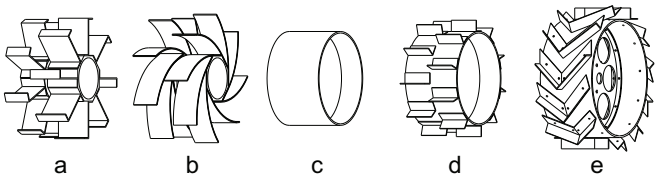

Fig. 6. The various wheel profiles that have been evaluated for the locomotion system.

The software is composed of a user interface on a host computer, onboard applications running on the CompactRio and CVS. The software was developed using NI LabVIEW 8.6.

B. Locomotion System Experiments

Numerous experiments have been done in order to test the effectiveness of the different proposed locomotion systems. Fig. 6 shows the five different wheels tested. From these, two main typologies can be observed: small diameter carcass with large length lugs or large diameter carcass with small length lugs. A brief description of these wheels is presented as follows:

- wheels **a** and **b** present different distribution of pressure over their surfaces;
- wheel **c** is only used as a reference;
- wheel **d** is used in order to compare carcass dimensions;
- wheel **e** is the largest and presents a different lug distribution w.r.t to wheel **d**.

The experiments have been performed at the San Rossore Regional Park (Pisa, Italy) that presents different types of sand terrain with different slopes. Experiments has shown that the simplified models that we have adopted to describe the wheel traction are sufficiently accurate, despite of their simplicity. Results can be summarized as follows:

1) Climbing: Climbing experiments are presented in Table I, where wheels were validated for different slope inclinations and different angular velocities. Tests were performed on slopes with a $2.4m$ path. Results report the following cases: accomplished task whenever the locomotion system is able to deal with the slope during the whole path; partially accomplished task whenever it can't accomplish the full path; or, failure. It can be verified that wheels within the big carcass typology presented the best results. Given that wheels **d** and **e** performed the best, Table II shows a more detailed analysis of these wheels where values for average speed during the task, total energy spent and total slip are presented for a $20°$ slope. From the table, it can be observed that even though wheel **e** presents higher slip, it can deal with the slope in all cases presented achieving higher speed with same energy consumption.

Moreover, Fig. 7 shows energy consumption as a function of slope inclinations for wheels **d** and **e**. The lines are a linear approximation of the data acquired during the tests. From the figure, it can be observed that wheel **e** presents lower consume and is able to deal with higher inclinations

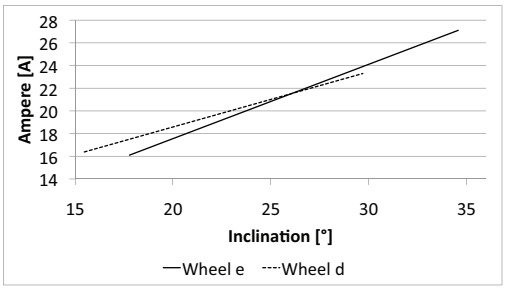

Fig. 7. Ampere vs Inclination for a $30°/s$

	$°/s$	a	b	c	d	e
$20°$	30	A	PA	PA	A	A
	60	PA	F	F	A	A
	120	F	F	F	PA	A
$30°$	30	PF	F	F	PA	A
	60	F	F	F	PA	PA
	120	F	F	F	F	F
$40°$	30	F	F	F	PA	PA
	60	F	F	F	F	F
	120	F	F	F	F	F

TABLE I
A: ACCOMPLISHED, PA: PARTIAL ACCOMPLISHED, F: FAILURE.

than wheel **d**. The standard deviation of the plot is $2.18A$ for wheel **e** and $1.99A$ for wheel **d**.

2) Flat terrain locomotion: Table III presents the flat terrain locomotion experiments done for wheels' angular velocities of $60°$ and $120°$. Tests were performed on a $9.4m$ track. Values for average speed during the task, total energy spent and total slip are presented for wheels **c**, **d** and **e**. Slippage values are similar for low velocity tests presenting higher dissimilarity for higher velocities. Wheel **e** presents the lowest slip, the lowest energy consumption and the best average speeds.

3) Maneuverability: With reference to Fig. 8, we have measured the drifts x and y for a $360°$ skid–steering turn. Results are reported in Table IV. As above it is clear that wheel **e** performed the best. Finally, wheels that performed properly during backward movement tests were: **c**, **d** and **e**.

		30 $[°/s]$	60 $[°/s]$	120 $[°/s]$
d	SP	0.03	0.13	X
	E	6	3	X
	S	22	20	X
e	SP	0.06	0.14	0.23
	E	6	3.2	3
	S	29	30	25

TABLE II
SP : SPEED $[m/s]$, E: ENERGY$[Wh]$, S: SLIP$[\%]$

	Test 1 Flat Terrain $[0,\ 70°]$ Motor Speed $60°/s$			Test 2 Flat Terrain $[0,\ 70°]$ Motor Speed $120°/s$		
	Speed	Energy	Slip	Speed	Energy	Slip
c	0.13	8.0	1.9	0.25	4.38	4.2
d	0.16	6.0	1.0	0.32	3.8	3.8
e	0.19	6.0	1.3	0.39	3.1	2.4

TABLE III
SPEED $[m/s]$, ENERGY$[Wh]$, SLIP$[\%]$

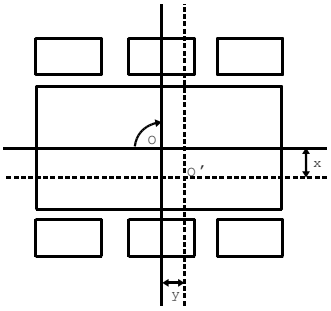

Fig. 8. Model adopted for maneuverability evaluation.

C. Casting System Experiments

Two sets of experiments have been designed to evaluate the performance of the casting system, and in particular to validate the dynamic model of Eq. 1 for the flight phase of the end–effector. The first set, S_1, involves initial throwing conditions of $\theta = 0$, $\alpha = 245°$, and $\dot{\alpha} = 1350\ °/s$, with an end–effector of 116 g. The second set, S_2, involves initial throwing conditions of $\theta = 0$, $\alpha = 265°$, and $\dot{\alpha} = 1200\ °/s$, with an end–effector of 388 g. During both types of experiments, the robotic end–effector is thrown by disengaging the clutch at the desired throwing configurations. During the entire flight, the clutch is completely disengaged, and thus only a residual torque τ due to friction is transmitted to the end–effector through the cable. A simple model for this torque can be obtained by assuming that τ is proportional to the velocity of the cable $\sqrt{\dot{x}^2 + \dot{y}^2 + \dot{z}^2}$ via a coefficient β.

By using S_1 as training set, the estimated value of β is 0.0576. The second set S_2 has then been used as a validation set of the casting system. Fig. 9 reports the results of both types of experiments. For the set S_1, the expected landing position of the end–effector, as determined by the dynamics in Eq. 1, is $p_e = (1.710, 0.255, 0)^T$ m, whereas the actual landing position is $\hat{p}_e = (1.583, 0.232, 0)^T$ m

	c	d	e
x	16	8	3
y	10	3	2

TABLE IV
DRIFT MEASURES IN $[cm]$.

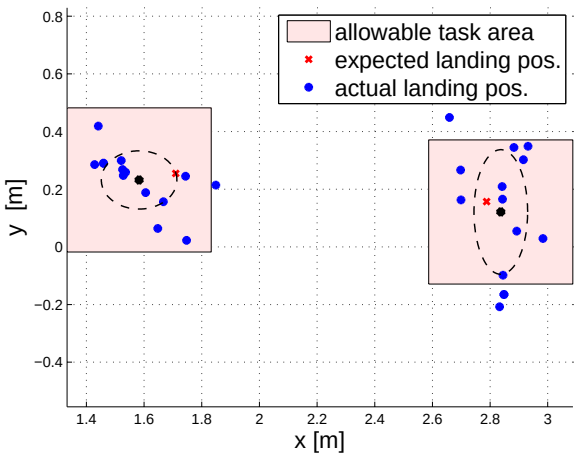

Fig. 9. Results of the two sets of experiments that have been designed for validating the casting system. The robot is placed at the origin of the system.

in average. The accuracy of the flight model w.r.t. the experiments S_1 can then be described by a bias $|p_e - \hat{p}_e|$ of $(0.1270, 0.0230, 0)^T$ m. Moreover, the precision of the casting system can be described by a standard deviation of 0.131 m along x, and of 0.101 m along y (see the dotted ellipse around $\hat{p}_e$). For the set S_2, the expected landing position of the end–effector is $p_e = (2.788, 0.157, 0)^T$ m, whereas the actual landing position is $\hat{p}_e = (2.837, 0.121, 0)^T$ m in average. The accuracy of the flight model w.r.t. the experiments S_2 can then be described by a bias $|p_e - \hat{p}_e|$ of $(0.0490, 0.0360, 0)^T$ m. Moreover, the precision of the casting system can be described by a standard deviation of 0.093 m along x, and of 0.216 m along y. According to the Challenge requirements, the sample soil is contained within a square region of 50 cm^2. Two red boxes around the means of the actual landing positions represent these allowable regions of successful sample acquisition, and are added in the figure only as a visual guide.

Another aspect that must be considered is the uncertainty in the throwing angle α, which obviously affects the landing position of the end–effector. In fact, the actual throwing angle $\hat{\alpha}$ may differ from the predicted one, due to delays in command transmission and in the actuation system that are not easy to compensate. Moreover, the effect of this uncertainty increases with the distance to be reached. Given a precision ϵ, as a maximum distance between the actual and the ideal landing position, the actual throwing angle $\hat{\alpha}$ must satisfy the constraint

$$-\arccos\left(1-\frac{\epsilon}{2(r^2+\delta^2)}\right) \leq \hat{\alpha} \leq \arccos\left(1-\frac{\epsilon}{2(r^2+\delta^2)}\right)$$

depending on the distance δ to be reached. Fig. 10 is a graphical representation of the above relation evaluated for different precision values. Our implementation of the system is able to release the end–effector at a throwing angle $\hat{\alpha} = \alpha \pm 6°$, where α is the theoretical value. According

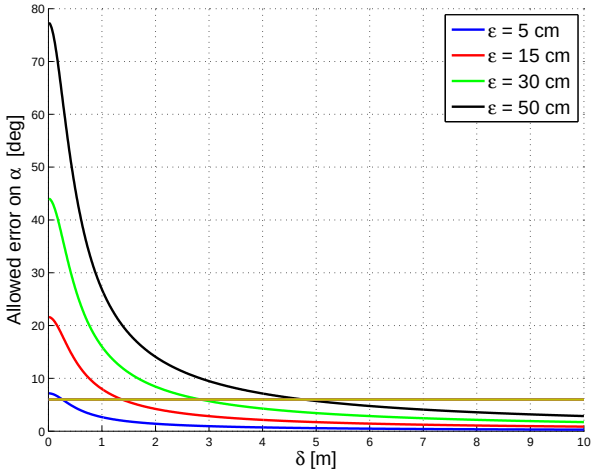

Fig. 10. Maximum allowed throwing angle error versus distance to be reached.

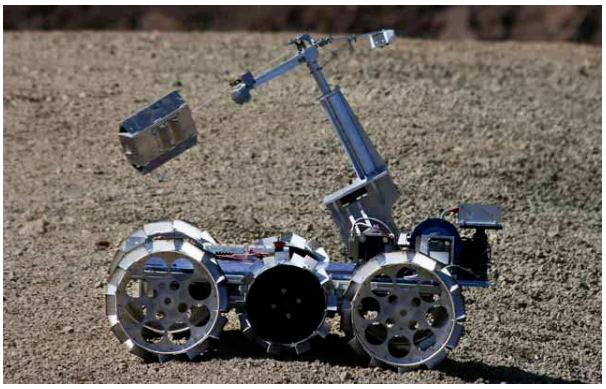

Fig. 11. Snapshot of DAVID, the University of Pisa Robotic System for the ESA Lunar Robotic Challenge, during a casting experiment at Tenerife Island.

to the Challenge requirements, to reach the sample with a maximum throwing angle error of $6°$, we can throw from a maximum distance of around 5.5 m (see Fig. 10).

V. Challenge Results and Final Discussion

Based on the considerations presented in II-A, and on the experimental results presented in IV-B, the final robot architecture is composed of four wheels of type **e**, mounted on the robot extremities, and two wheels of type **d**, mounted in the center of the robot frame. This structure allows to low energy consumption on soft slopes, a good obstacle negotiation capacity and good pressure distribution on slopes of higher inclination. During tests and at the challenge, the locomotion system proved to be able to accomplish the required mission: the vehicle was able to negotiate inclines of up to 40 degrees during both descending and ascending tasks. Inside the crater, the vehicle showed good maneuverability and low slippage. Moreover, it was able to deal with obstacles with dimensions of around 30 cm. Due to malfunctioning of a component of the casting system few hours before the Challenge, and the impossibility to replace it in short time, the casting system was not used during the Challenge. Instead an alternative mechanism that we do not describe here for space reasons was used. However, its operation was later tested at the Challenge site, which showed that the casting manipulator to be adequate for the task. A snapshot of DAVID during a casting experiment at Tenerife Island is reported in Fig. 11.

This paper describes the developed architecture for a lunar robot designed to compete in the 2008 ESA Lunar Robotics Challenge. More specifically, the locomotion system and the sample retrieval system were presented. The most innovative aspect of our approach is the casting manipulator that was used to retrieve soil samples. Both systems were tested and experiments showed their effectiveness. The rover developed for the challenge provides a modular platform that can be used for future research with mobile robots; more specifically, the casting system presents interesting challenges that can motivate new research on this kind of manipulator.

VI. Acknowledgment

The authors wish to thank Fabrizio Flacco, Rino L'Episcopia, Gaetano Lorefice, Federico Puccinelli, Andrea Di Basco, Manolo Garabini, Michael Catanzaro, Fabrizio Vivaldi and Nicola Di Lecce for their contributions to the development of the project as well as the successful result of the competition.

References

[1] Hitoshi Arisumi, Tetsuo Kotoku, and Kiyoshi Komoriya. Swing motion control of casting manipulation. *IEEE Control Systems*, 1999.

[2] M.G. Bekker. *Theory of Land Locomotion*. University of Michigan Press, Ann Arbor, MI, 1956.

[3] M.G. Bekker. *Introduction to Terrain-Vehicle Systems*. University of Michigan Press, Ann Arbor, MI, 1969.

[4] Adriano Fagiolini, Hitoshi Arisumi, and Antonio Bicchi. Visual-based feedback control of casting manipulation. *Proc. IEEE International Conference on Robotics and Automation*, pages 2203–2208, 2005.

[5] O. Khatib, K. Yokoi, K. Chang, D. Ruspini, R. Holmberg, and A. Casal. Vehicle/arm coordination and multiple mobile manipulator decentralized cooperation. *Proc. IEEE International Conference on Intelligent Robots and Systems*, 1996.

[6] Rolf Mamen. Applying space technologies for human benefit: the canadian experience and global trends. *Canadian Space Agency*, 2003.

[7] J.Y. Wong. *Terramechanics and Off-road Vehicles*. Wiley-Interscience, New York, 1989.